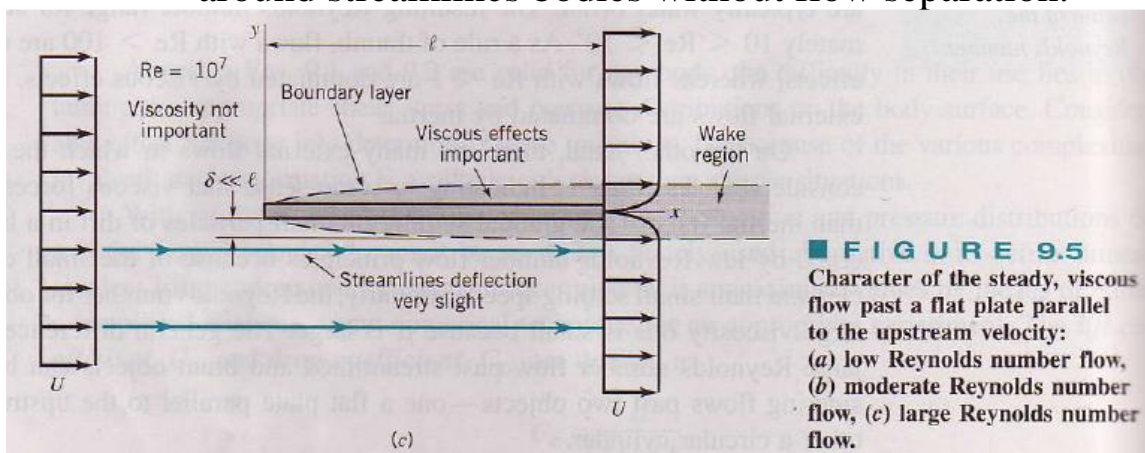


Chapter 7.4 Bluff Body

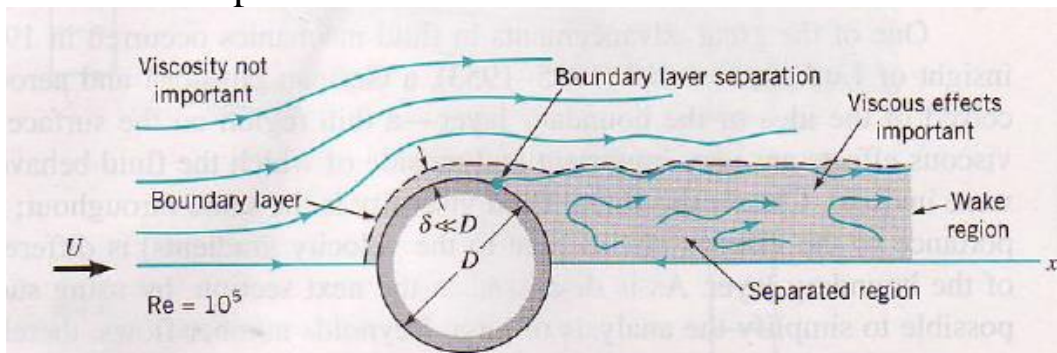
Fluid flows are broadly categorized:

1. Internal flows such as ducts/pipes, turbomachinery, open channel/river, which are bounded by walls or fluid interfaces: Chapter 6.
2. External flows such as flow around vehicles and structures, which are characterized by unbounded or partially bounded domains and flow field decomposition into viscous and inviscid regions: Chapter 7.

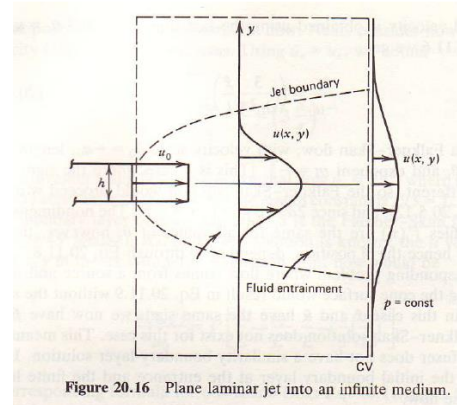
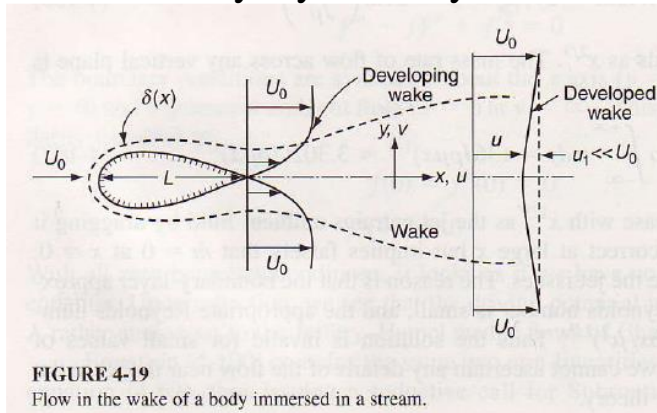
- a. Boundary layer flow: high Reynolds number flow around streamlines bodies without flow separation.



- b. Bluff body flow: flow around bluff bodies with flow separation.

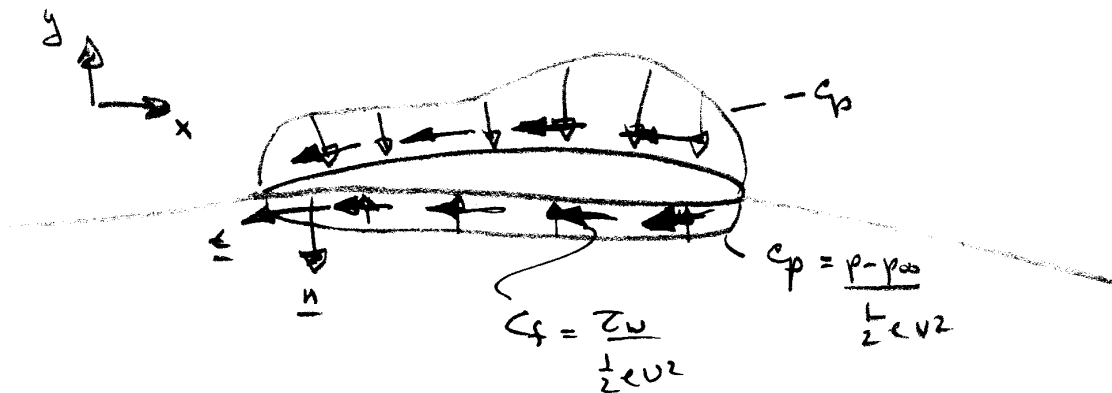


3. Free Shear flows such as jets, wakes, and mixing layers, which are also characterized by absence of walls and development and spreading in an unbounded or partially bounded ambient domain: advanced topic, which also uses boundary layer theory.



Basic Considerations

Drag is decomposed into form and skin-friction contributions:



$$C_D = \frac{1}{\frac{1}{2} \rho V^2 A} \left\{ \underbrace{\int_S (p - p_\infty) \underline{n} \cdot \hat{i} dA}_{C_{Dp}} + \int_S \tau_w \underline{t} \cdot \hat{i} dA \right\}_{C_f}$$

$$C_L = \frac{1}{\frac{1}{2}\rho V^2 A} \left\{ \int_S (p - p_\infty) \underline{n} \cdot \hat{j} dA \right\}$$

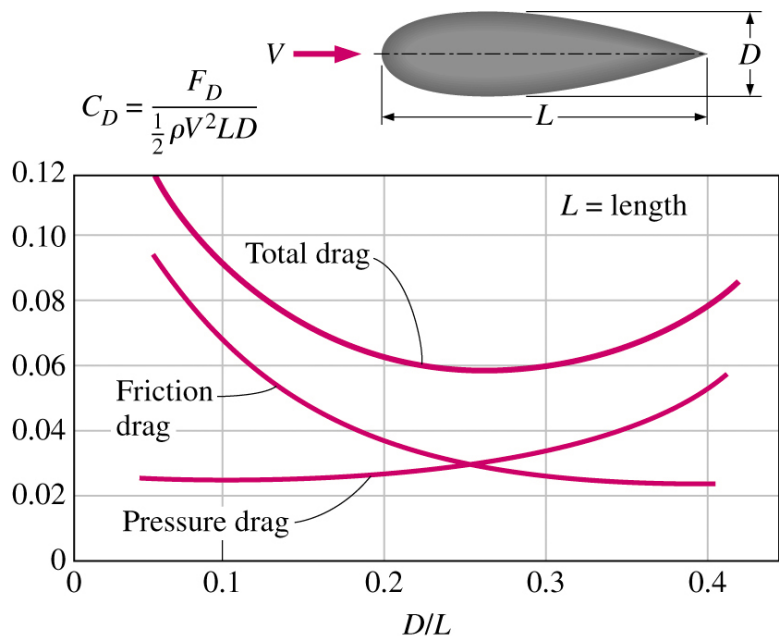
$\frac{t}{c} \ll 1 \quad C_f \gg C_{Dp} \quad \text{streamlined body}$

$\frac{t}{c} \sim 1 \quad C_{Dp} \gg C_f \quad \text{bluff body}$

Streamlining: One way to reduce the drag

- reduce the flow separation → reduce the pressure drag
- increase the surface area → increase the friction drag

→ **Trade-off relationship** between pressure drag and friction drag



Trade-off relationship between pressure drag and friction drag

Benefit of streamlining: reducing vibration and noise

Drag of 2-D Bodies

First consider a flat plate both parallel and normal to the flow

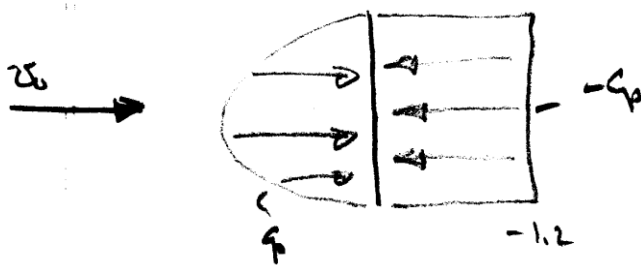


$$C_{Dp} = \frac{1}{\frac{1}{2}\rho V^2 A^s} \int (p - p_\infty) \underline{n} \cdot \underline{i} = 0$$

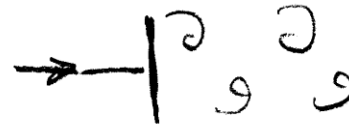
$$C_f = \frac{1}{\frac{1}{2}\rho V^2 A^s} \int \tau_w \underline{t} \cdot \hat{\underline{i}} dA$$

$$= \frac{1.33}{Re_L^{1/2}} \quad \text{laminar flow}$$

$$= \frac{.074}{Re_L^{1/5}} \quad \text{turbulent flow}$$



flow pattern



vortex wake
 typical of bluff body flow

where C_p based on experimental data

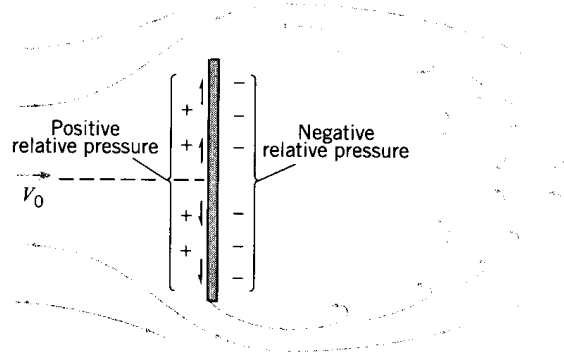
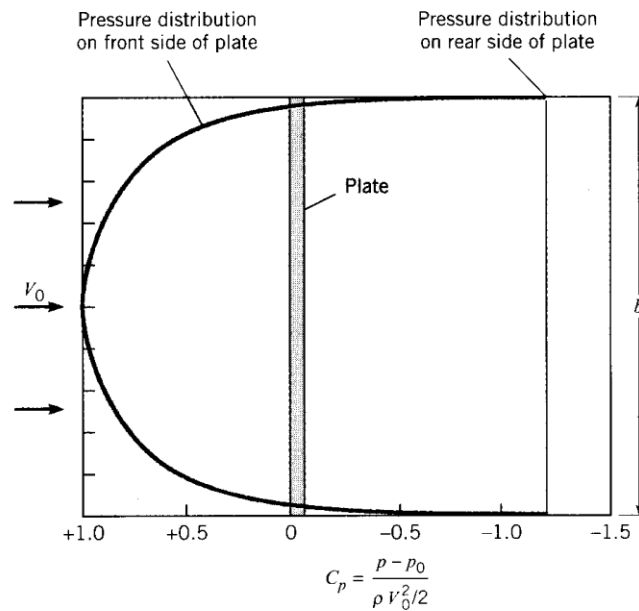


FIGURE 11.3
Flow past a flat plate.

FIGURE 11.4
Pressure distribution on a plate normal to the approach flow for $Re > 10^4$.



$$C_{Dp} = \frac{1}{\frac{1}{2}\rho V^2 A^s} \int (p - p_\infty) \underline{n} \cdot \hat{i} dA$$

$$= \frac{1}{A_s} \int C_p dA$$

$= 2$ using numerical integration of experimental data
 $C_f = 0$

For bluff body flow experimental data used for C_D .

In general, Drag = $f(V, L, \rho, \mu, c, t, \varepsilon, T, \text{etc.})$
 from dimensional analysis

$$C_D = \frac{\text{Drag}}{\frac{1}{2}\rho V^2 A} = f\left(\text{Re}, \text{Ar}, \frac{t}{L}, \frac{\varepsilon}{L}, T, \text{etc.}\right)$$

\swarrow c/L
 $\underbrace{\hspace{10em}}_{\text{scale factor}}$

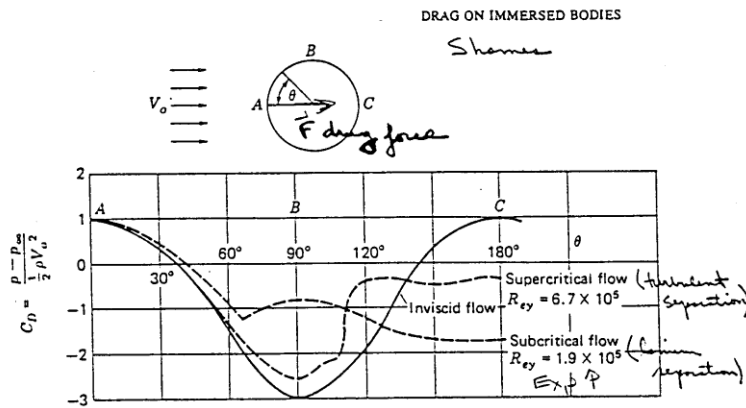


Figure 10.23 Pressure distributions around a cylinder for subcritical, supercritical, and inviscid flows.

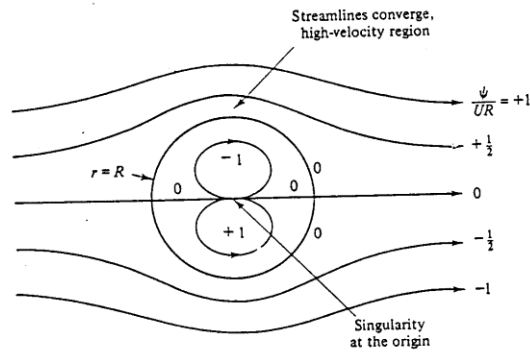


Fig. E4.7

Potential Flow Solution: $\psi = -U_\infty \left(r - \frac{a^2}{r} \right) \sin \theta$

$$p + \frac{1}{2} \rho V^2 = p_\infty + \frac{1}{2} \rho U_\infty^2 \qquad u_r = \frac{1}{r} \frac{\partial \psi}{\partial \theta}$$

$$C_p = \frac{p - p_\infty}{\frac{1}{2} \rho U_\infty^2} = 1 - \frac{u_r^2 + u_\theta^2}{U_\infty^2} \qquad u_\theta = -\frac{\partial \psi}{\partial r}$$

$$C_p(r = a) = 1 - 4 \sin^2 \theta \longleftarrow \text{surface pressure}$$

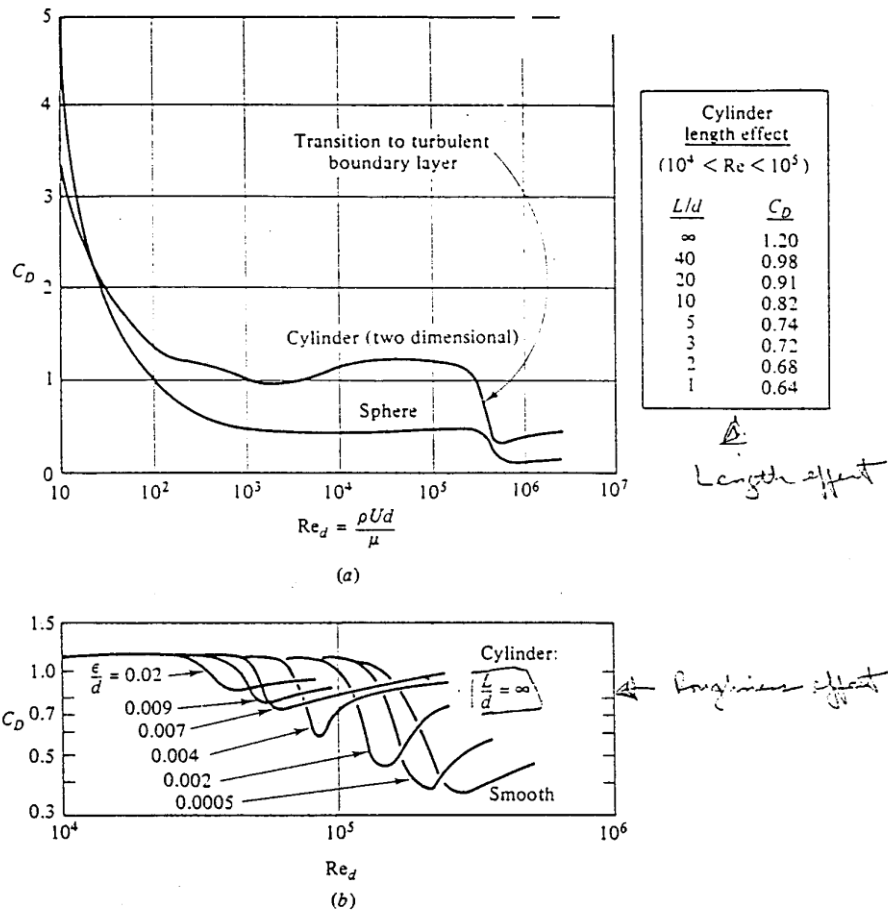


Fig. 5.3 The proof of practical dimensional analysis: drag coefficients of a cylinder and sphere: (a) drag coefficient of a smooth cylinder and sphere (data from many sources); (b) increased roughness causes earlier transition to a turbulent boundary layer.

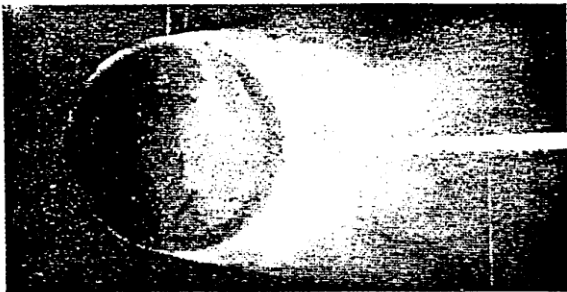


FIG. 34.—Flow round sphere below critical point. (Wieselsberger.)

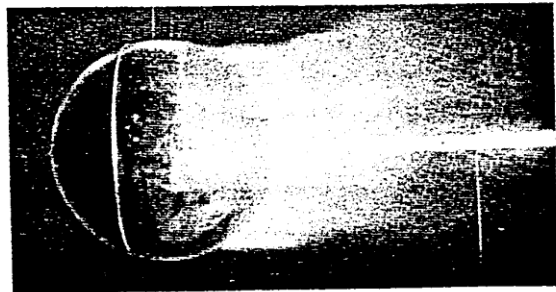


FIG. 35.—Owing to a thin wire ring round the sphere, the flow becomes of the other type with turbulent boundary layer. (Wieselsberger.)

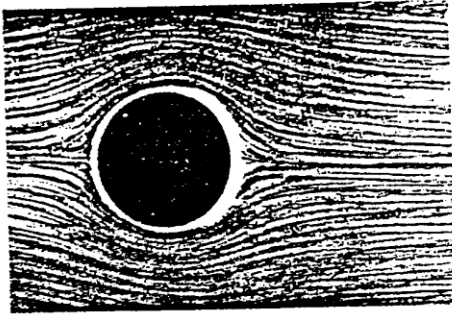


Fig. 15.5a

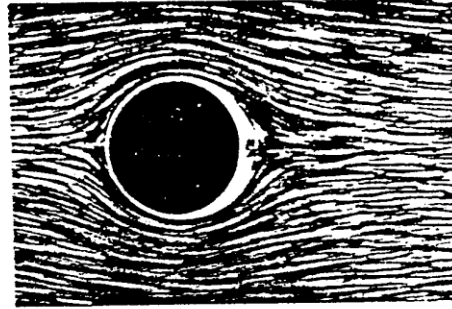


Fig. 15.5b

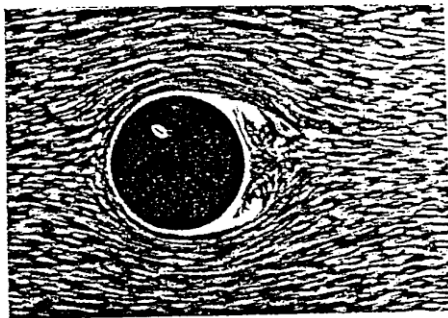


Fig. 15.5c

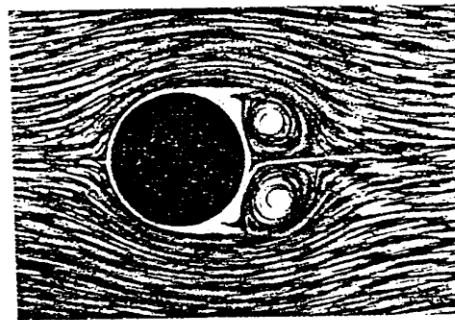


Fig. 15.5d

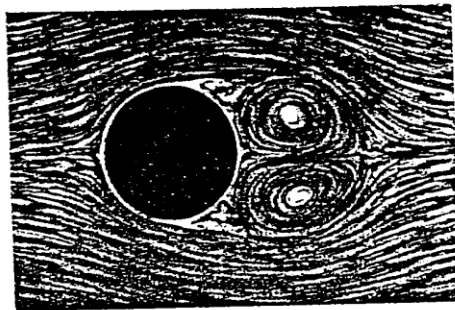


Fig. 15.5e

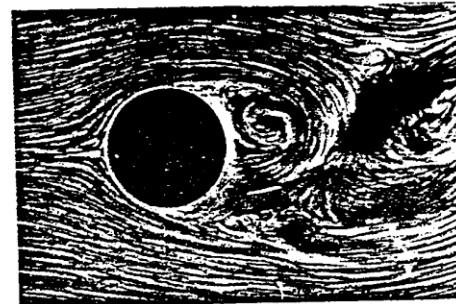
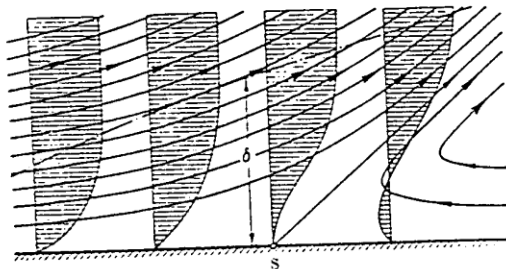


Fig. 15.5f

Fig. 15.5 a to f. Formation of vortices in flow past a circular cylinder after acceleration from rest (L. Prandtl)



S = point of separation

Fig. 2.12. Diagrammatic representation of flow in the boundary layer near a point of separation

alternate formation and shedding of vortices also creates a regular change in pressure with consequent periodicity in side thrust on the cylinder. Vortex shedding was the primary cause of failure of the Tacoma Narrows suspension bridge in the state of Washington in 1940. Another, more commonplace, effect of vortex shedding is the “singing” of wires in the wind.

If the frequency of the vortex shedding is in resonance with the natural frequency of the member that produces it, large amplitudes of vibration with consequent large stresses can develop. Experiments show that the frequency of shedding is given in terms of the Strouhal number S , and this in turn is a function of the Reynolds number. Here the Strouhal number is defined as

$$S = \frac{nd}{V_0} \quad (11-7)$$

where n is the frequency of shedding of vortices from one side of cylinder, in Hz, d is the diameter of cylinder, and V_0 is the free-stream velocity.

The relationship between the Strouhal number and the Reynolds number for vortex shedding from a circular cylinder is given in Fig. 11-10.

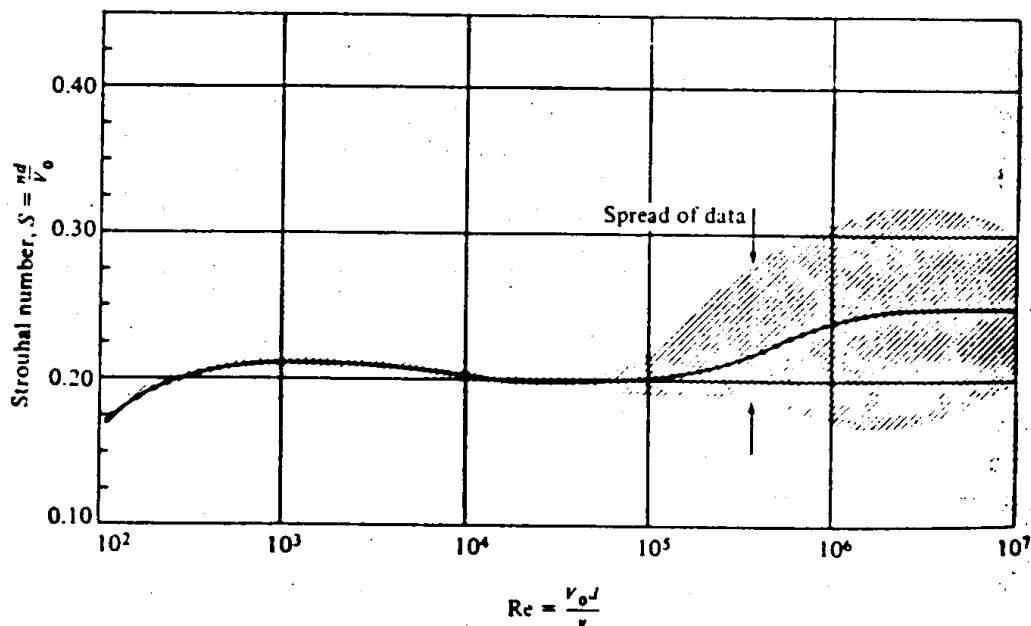


FIGURE 11-10 Strouhal number versus Reynolds number for flow past a circular cylinder. [After Jones (14) and Roshko (23)]

Other cylindrical and two-dimensional bodies also shed vortices. Consequently, the engineer should always be alert to vibration problems when designing structures that are exposed to wind or water flow.

EXAMPLE 11-2 For the cylinder and conditions of Example 11-1, at what frequency will the vortices be shed?

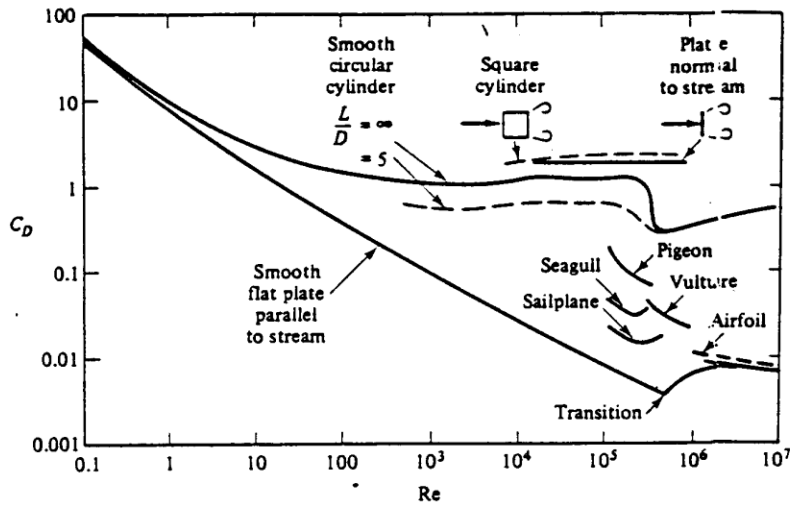


Fig. 7.16 Drag versus Reynolds number for nearly two-dimensional bodies.

Table 7.2

DRAG OF TWO-DIMENSIONAL BODIES AT $Re = 10^5$

Shape	C_D based on frontal area	Shape	C_D based on frontal area
Plate:		Half-cylinder:	
	2.0		1.2
Square cylinder:			
	2.1		1.7
	1.6	Equilateral triangle:	
Half tube:			1.6
	1.2		2.0
	2.3		
Elliptical cylinder:			
		<u>Laminar</u>	<u>Turbulent</u>
1:1	1.2	0.3	
2:1	0.6	0.2	
4:1	0.35	0.15	
8:1	0.25	0.1	

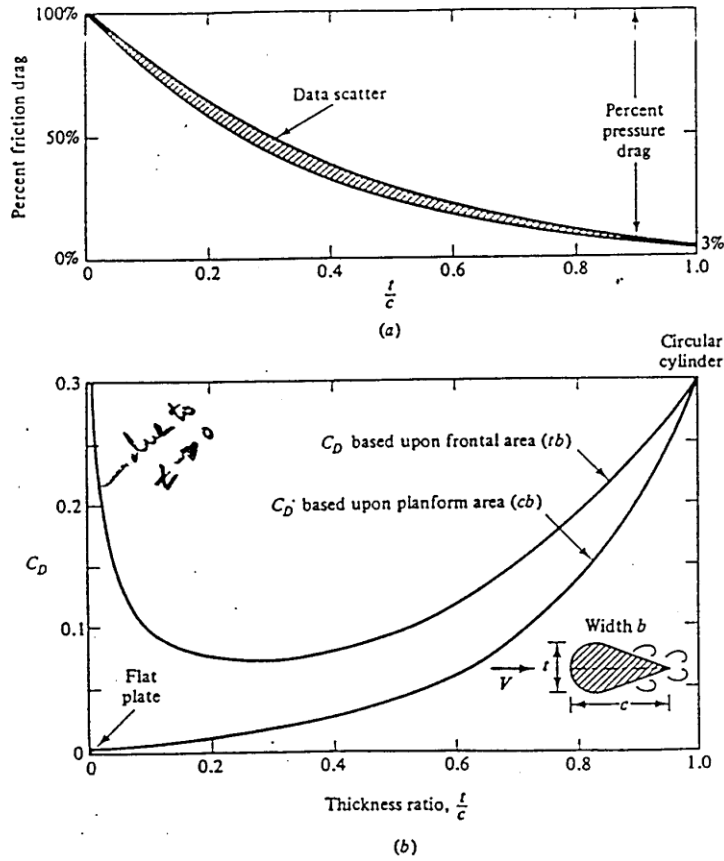


Fig. 7.12 Drag of a streamlined two-dimensional cylinder at $Re_c = 10^6$: (a) effect of thickness ratio on percentage friction drag; (b) total drag versus thickness when based upon two different areas.

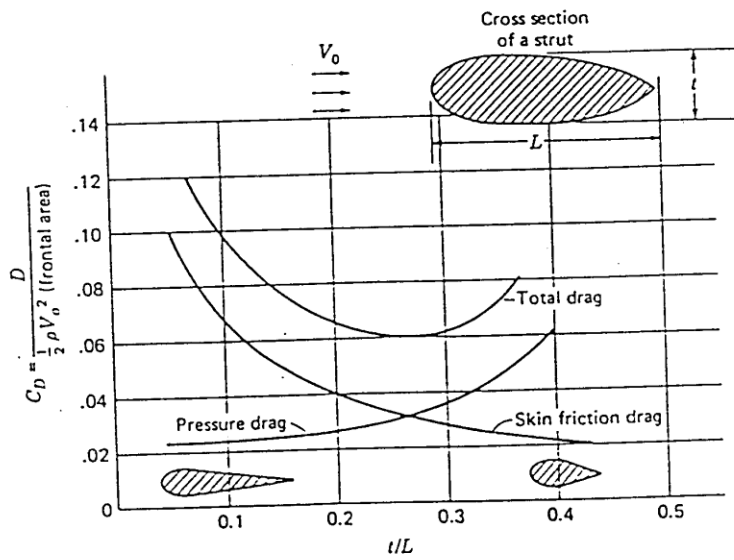


Figure 10.24 Drag coefficients for a family of struts. (S. Goldstein, "Modern Developments in Fluid Dynamics," Dover Publications, New York, 1965.)

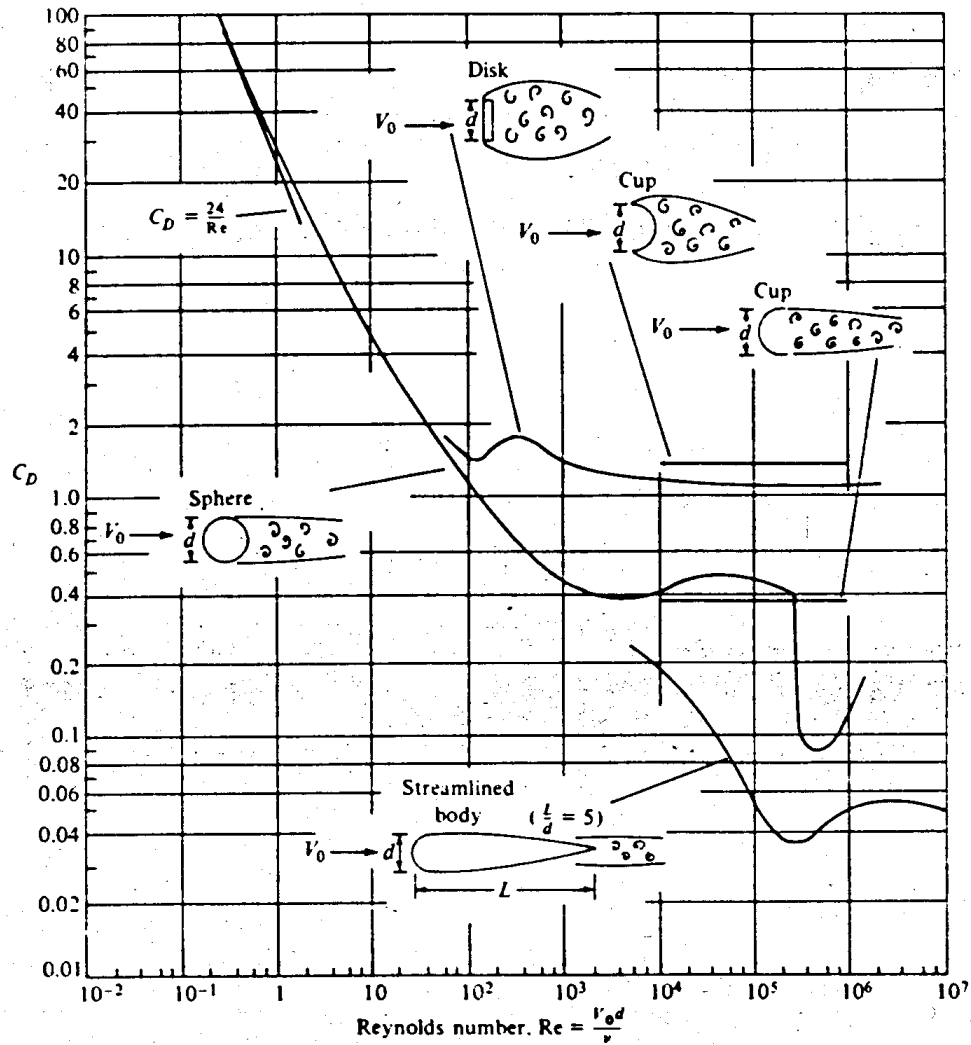
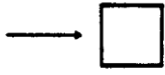
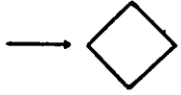
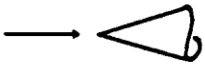
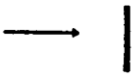
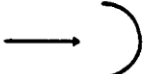
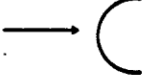

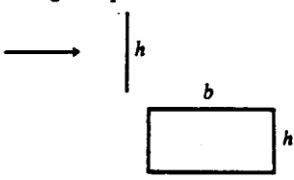
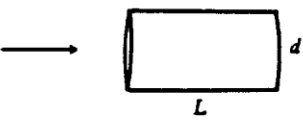
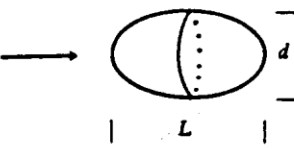


FIGURE 11-11 Coefficient of drag versus Reynolds number for axisymmetric bodies. [Data sources: Abbott (1), Breevoort (4), Freeman (9), and Rouse (24).]

Table 7.3
DRAG OF THREE-DIMENSIONAL BODIES AT $Re \approx 10^5$

Body	Ratio	C_D based on frontal area		
Cube: 		1.07		
		0.81		
60° cone: 		0.5		
Disk: 		1.17		
Cup: 		1.4		
		0.4		
Parachute (low porosity): 		1.2		
Rectangular plate: 	b/h	1	1.18	
		5	1.2	
		10	1.3	
		20	1.5	
		∞	2.0	
Flat-faced cylinder: 	L/d	0.5	1.15	
		1	0.90	
		2	0.85	
		4	0.87	
		8	0.99	
Ellipsoid: 	L/d	0.75	0.5	0.2
		1	0.47	0.2
		2	0.27	0.13
		4	0.25	0.1
		8	0.2	0.08

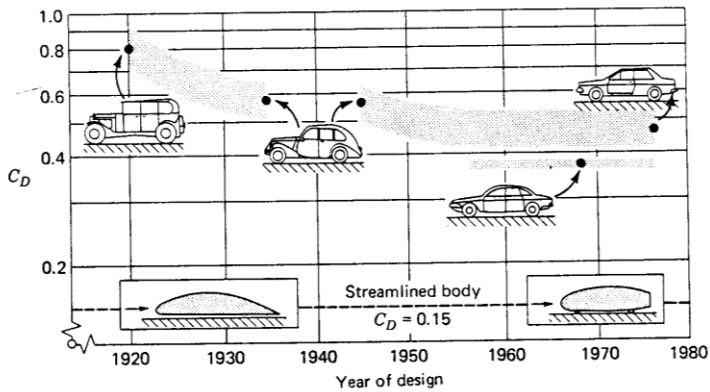


Figure 10.25 Time history of the aerodynamic drag of cars in comparison with streamlined bodies. (From Hucho, W. H., Janssen, L. J., Emmelmann, H. J., 1976, "The Optimisation of Body Details—A Method For Reducing The Aerodynamic Drag of Road Vehicles," SAE 760185.)

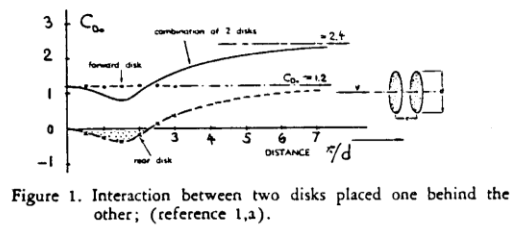
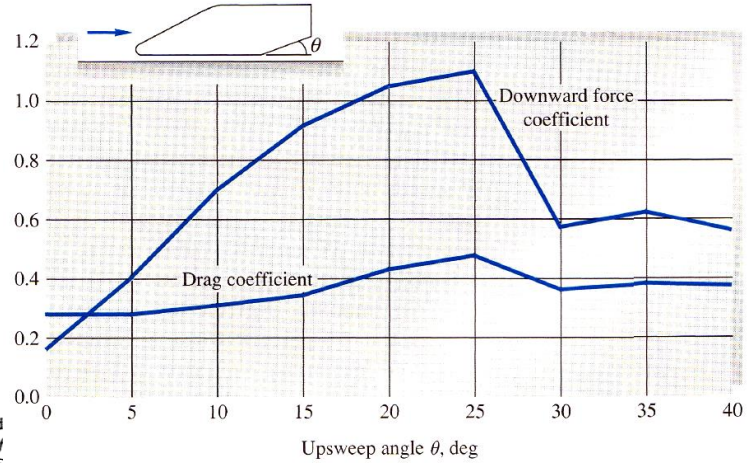


Figure 1. Interaction between two disks placed one behind the other; (reference 1,2).

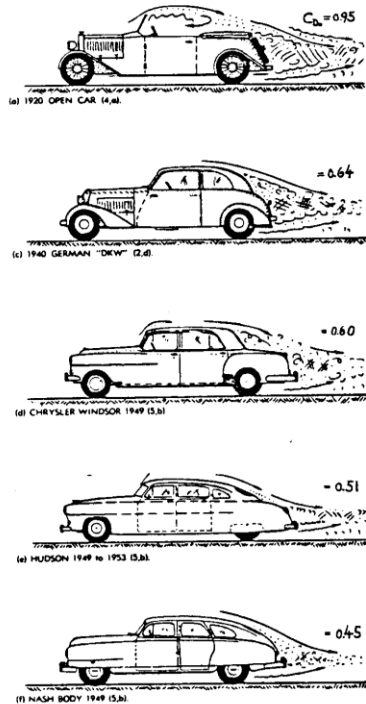


Figure 3. Drag coefficients of "standard" passenger cars, tested either in wind tunnels on geometrically similar models or by deceleration of the full-scale vehicle.

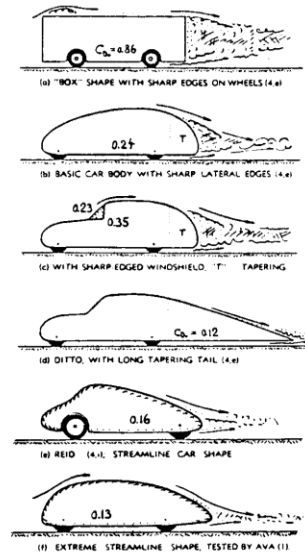


Figure 4. Drag coefficients of several smooth wind tunnel models (tested over fixed ground plate).

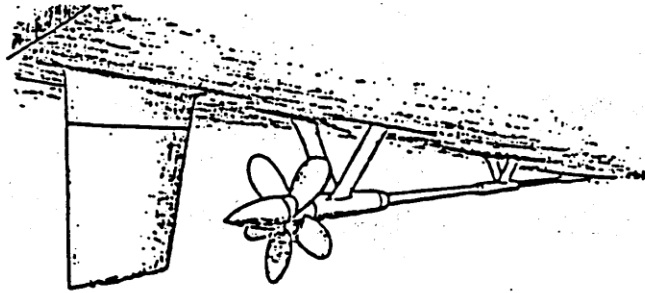


Figure 2-4. Typical naval ship stern appendages (from Kirkman, et al., 1979)

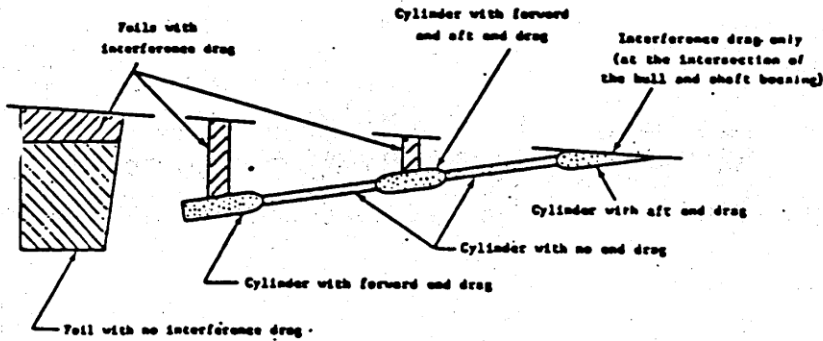


Figure 2-5. Appendage decomposition (from Kirkman, et al., 1979)

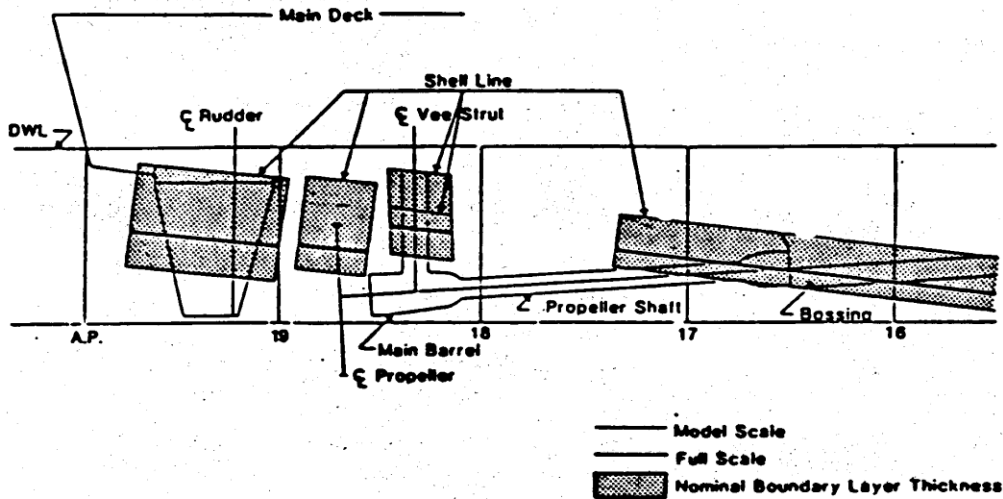


Figure 2-6. Nominal boundary layer thickness in way of the DDG 51 appendages.

Effect of Compressibility on Drag: $C_D = C_D(Re, Ma)$

$$Ma = \frac{U_\infty}{a}$$

speed of sound = rate at which infinitesimal disturbances are propagated from their source into undisturbed medium

$Ma < 1$	subsonic	≤ 0.3 flow is incompressible,
$Ma \sim 1$	transonic (=1 sonic flow)	i.e., $\rho \sim \text{constant}$
$Ma > 1$	supersonic	
$Ma \gg 1$	hypersonic	

C_D increases for $Ma \sim 1$ due to shock waves and wave drag

$Ma_{\text{critical}}(\text{sphere}) \sim .6$

$Ma_{\text{critical}}(\text{slender bodies}) \sim 1$

For $U \geq a$: upstream flow is not warned of approaching disturbance which results in the formation of shock waves across which flow properties and streamlines change discontinuously

FIGURE 11.12
 Drag characteristics of
 projectile, sphere, and
 cylinder with
 compressibility effects.
 [After Rouse (26)]

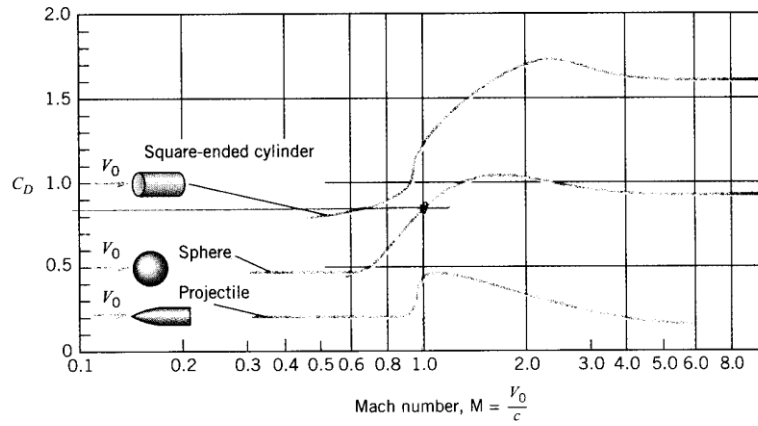


FIGURE 11.13
 Contour plot of the drag
 coefficient of the sphere
 versus Reynolds and
 Mach numbers.

